

---

---

# Comparison of Medium- and High-Energy Collimators for $^{131}\text{I}$ -Tositumomab Dosimetry

Eugene Mah and Ken M. Spicer

Department of Radiology, Medical University of South Carolina, Charleston, South Carolina

---

Residence time measurements obtained by serial whole-body conjugate-view imaging are commonly used in patient-specific dosimetry for radioimmunotherapy applications. In order to determine the effect of collimator selection on residence time measurements for  $^{131}\text{I}$ , the accuracies of  $^{131}\text{I}$  half-life measurements obtained with multiple  $\gamma$ -camera and collimator combinations were investigated. **Methods:** Serial anterior and posterior whole-body images were acquired over a period of 15 d with 4 different  $\gamma$ -cameras and medium- or high-energy collimators. Background-corrected geometric mean counts from the images were fitted to a monoexponential curve to determine the half-life of  $^{131}\text{I}$  obtained with the different  $\gamma$ -camera and collimator combinations. **Results:** An average half-life of 8.15 d (SD, 0.07 d) was obtained with all  $\gamma$ -camera and collimator combinations. A half-life of 8.12 d (SD, 0.11 d) was obtained with the high-energy collimators, and a half-life of 8.18 d (SD, 0.04 d) was obtained with the medium-energy collimators. These values are all very close to the  $^{131}\text{I}$  physical half-life of 8.02 d and were not found to be statistically significantly different ( $P = 0.44$ ). Similar results were obtained for the half-life obtained with single-head  $\gamma$ -camera configurations (mean half-life, 8.15 d; SD, 0.12 d). The therapeutic  $^{131}\text{I}$ -tositumomab dose resulting from the differences in the measured half-life ranged from 2.58 to 2.6 GBq (69.8–70.4 mCi). **Conclusion:** There is no significant difference in  $^{131}\text{I}$  half-life and residence time measurements obtained with medium- or high-energy collimators in dual-head or single-head imaging configurations.

**Key Words:**  $^{131}\text{I}$  half-life; medium-energy collimators; high-energy collimators; radioimmunotherapy

**J Nucl Med Technol 2007; 35:148–153**

DOI: 10.2967/jnmt.106.038174

---

In most applications, the primary goal of radioimmunotherapy (RIT) imaging is to perform absolute quantitation of organ activity for the purposes of determining organ dose for the therapeutic portion of the procedure. Ideally, RIT imaging would be performed with 3-dimensional imaging methods, such as SPECT and CT, to obtain volumetric information about the distribution of the therapeutic agent within the body (1,2). Corrections for attenuation, scatter,

collimator effects, and organ size would be required for quantitative RIT dosimetry (1,3,4). In practice, however, performing all of these corrections is time-consuming, labor-intensive, and impractical for many institutions and clinics. Further, the marginally improved organ dose is unlikely to result in a demonstrably improved therapeutic outcome.

Whole-body conjugate-view imaging is an established method for quantifying the amount of activity remaining in the body or in various organs for RIT dosimetry applications (5,6). In the simplified technique described by Wahl et al. (5), a small dose of a radiotracer-labeled monoclonal antibody is administered to the patient intravenously. Serial whole-body imaging is conducted over a period of 6–7 d to obtain measurements of the whole-body radiopharmaceutical clearance rate. From these measurements, total body retention time (TBRT) is calculated; TBRT then is used to determine the maximal nontoxic amount of activity for an optimal therapeutic dose.

For  $^{131}\text{I}$  RIT imaging, such as the conjugate-view imaging used for  $^{131}\text{I}$ -tositumomab administration, high-energy collimators are normally used, because the primary  $\gamma$ -rays have an energy of 364 keV (with secondary, less abundant  $\gamma$ -rays at 637 and 723 keV). Because of the high-energy  $\gamma$ -rays emitted, the use of medium-energy collimators for imaging has not been recommended to date, because of a perception that excessive septal penetration may affect the ability to accurately assess TBRT. The purposes of serial whole-body imaging are to measure the relative amount of activity remaining in the body and to determine the TBRT for the patient, rather than radioactivity quantitation. Consequently, systematic errors resulting from effects such as septal penetration and collimator sensitivity are removed (assuming that acquisition parameters and patient positioning remain the same between imaging sessions). Septal penetration and collimator sensitivity would affect direct measurements of activity (the  $y$ -intercept of the time–activity curve) but not residence time measurements (the slope of the time–activity curve). In theory, TBRT would not be expected to be discrepant whether measured with medium- or high-energy collimators. In this study, we attempted to verify this notion by using both high- and medium-energy collimators to measure the physical half-life of  $^{131}\text{I}$  in a phantom and by using the  $^{131}\text{I}$  half-life as a substitute for TBRT, because measurements of the 2 quantities are directly related.

---

Received Nov. 14, 2006; revision accepted Feb. 21, 2007.

For correspondence or reprints contact: Eugene Mah, Department of Radiology, Medical University of South Carolina, Box 250322, Charleston, SC 29425.

E-mail: maheug@musc.edu

COPYRIGHT © 2007 by the Society of Nuclear Medicine, Inc.

Imaging also serves to identify any alterations in the normal biodistribution of the RIT agent. Although image resolution and contrast are expected to be different with medium- and high-energy collimators, the task of visualizing altered biodistribution is generally not one that requires the detection of low-contrast changes or high spatial resolution. Altered biodistribution is generally characterized by high-contrast changes in activity distribution, so as long as image contrast is adequate with both medium- and high-energy collimators, the ability to visualize altered biodistribution should not be impaired.

## MATERIALS AND METHODS

To determine the half-life of  $^{131}\text{I}$ , serial measurements of phantoms containing  $\text{Na}^{131}\text{I}$  were obtained with several different  $\gamma$ -cameras and collimators. Three different phantoms were used for this study: an anthropomorphic chest phantom (Data Spectrum Corp.), an abdominal torso phantom (Phantom Laboratory), and a contrast-detail phantom (Rollo phantom). The various chambers of the phantoms were filled from an  $^{131}\text{I}$  stock solution having a concentration of 37 MBq/100 mL (1 mCi/100 mL). Two spheres, 3 and 6 cm in diameter, were used in the abdominal torso phantom to simulate abnormal biodistribution and were filled with activity concentrations of 185 and 74 MBq/mL (5 and 2 mCi/mL), respectively. Tables 1 and 2 show the activity distributions in the various chambers of the phantoms used. The total activity in the chest and torso phantoms was approximately 99 MBq (2.7 mCi). The contrast-detail phantom was filled with water, and 37 MBq (1 mCi) of  $^{131}\text{I}$  were added.

Imaging was performed with 4 different  $\gamma$ -cameras (GE Millennium VG [GE Healthcare], Philips Skylight [ $n = 2$ ], and Philips Vertex V60) and medium-energy general-purpose (MEGP) or high-energy general-purpose (HEGP) collimators. The  $\gamma$ -camera and collimator combinations used are provided in Table 3. Three sets of measurements were obtained with medium-energy collimators, and 2 sets of measurements were obtained with high-energy collimators. Collimator specifications for some of the systems are provided in Table 4. The GE Millennium VG camera was equipped with 15.9-mm-thick NaI crystals, whereas the Philips cameras were equipped with standard 9.5-mm-thick NaI crystals.

Anterior and posterior whole-body images were acquired with the same acquisition protocol as that described for  $^{131}\text{I}$ -tositumomab by Wahl et al. (5). Imaging was performed at 2, 45, 120, 138, 167, 188, and 285 h after the administration of activity into the phantoms. For each  $\gamma$ -camera and collimator combination, a whole-body acquisition was obtained with all 3 phantoms placed together on the table. Anterior and posterior whole-body images were acquired over

**TABLE 1**  
Chest Phantom Activity Distribution

| Chamber               | Volume (L) | Activity concentration (MBq/L) | Total activity (MBq) |
|-----------------------|------------|--------------------------------|----------------------|
| Liver                 | 1.175      | 6.30                           | 7.4                  |
| Lungs                 | 0.787      | 4.70                           | 3.7                  |
| Heart (outer chamber) | 0.116      | 63.8                           | 7.4                  |
| Thorax                | 8.4        | 2.2                            | 18.5                 |

**TABLE 2**  
Abdominal Phantom Activity Distribution

| Chamber     | Volume (L) | Activity concentration (MBq/L) | Total activity (MBq) |
|-------------|------------|--------------------------------|----------------------|
| Liver       | 1.475      | 6.27                           | 9.25                 |
| 6-cm sphere | 0.113      | 74                             | 8.4                  |
| 3-cm sphere | 0.014      | 37                             | 2.6                  |
| Thorax      | 8.23       | 1.12                           | 48.7                 |

a 195-cm scan length at a scan speed of 20 cm/min with 20% energy windows centered around 364 keV. Anterior head height was set to approximately 2 cm above the phantom. This distance was maintained for all subsequent scans. After the scans, the phantoms were removed, and a background scan was acquired with the same parameters.

From each imaging session, the total counts were obtained from the anterior and posterior phantom and background images. The background-corrected geometric mean counts ( $C$ ) were computed by subtracting the anterior and posterior counts from the background images ( $B_{\text{ant}}$  and  $B_{\text{post}}$ , respectively) and the anterior and posterior counts from the phantom images ( $C_{\text{ant}}$  and  $C_{\text{post}}$ , respectively), multiplying the resulting 2 counts, and taking the square root, as follows:

$$C = \sqrt{(C_{\text{ant}} - B_{\text{ant}}) \times (C_{\text{post}} - B_{\text{post}})}. \quad \text{Eq. 1}$$

The background-corrected geometric mean counts were recorded and plotted against the elapsed time from the initial activity calibration to produce a set of time-activity curves for each  $\gamma$ -camera and collimator combination. These data were used to determine exponential equations of best fit of the form

$$A(t) = A_0 \exp(-\lambda t) \quad \text{Eq. 2}$$

with Microsoft Excel (Microsoft Corp.); in this equation,  $A(t)$  is activity at time  $t$ ,  $A_0$  is initial activity (activity at time  $t = 0$ ), and  $-\lambda t$  is product of decay constant and time. From these calculated fit parameters, the half-life of  $^{131}\text{I}$  for each  $\gamma$ -camera and collimator combination was obtained as follows:

$$t_{1/2} = \frac{\ln 2}{\lambda}. \quad \text{Eq. 3}$$

A similar analysis was performed for anterior-only and posterior-only images to investigate whether there was any difference in the measured  $^{131}\text{I}$  half-life for single-head  $\gamma$ -cameras. An analysis of the measured half-lives at the 2 NaI crystal thicknesses (15.9

**TABLE 3**  
 $\gamma$ -Camera and Collimator Combinations

| Collimator | GE Millennium VG | Philips Skylight 1 | Philips Skylight 2 | Philips Vertex V60 |
|------------|------------------|--------------------|--------------------|--------------------|
| MEGP       | X                | X                  |                    | X                  |
| HEGP       | X                |                    | X                  |                    |

**TABLE 4**  
Collimator Specifications

| Collimator            | Hole diameter (mm) | Hole length (mm) | Septal thickness (mm) | Septal penetration (%) | Septal penetration (keV) |
|-----------------------|--------------------|------------------|-----------------------|------------------------|--------------------------|
| Skylight MEGP         | 2.95               | 48               | 1.143                 | 3.3                    | 300                      |
| Skylight HEGP         | 3.81               | 60               | 1.727                 | 3.5                    | 364                      |
| Vertex V60 MEGP       | 2.95               | 48               | 1.143                 | 3.3                    | 300                      |
| GE Millennium VG MEGP | 3.0                | 58               | 1.05                  |                        |                          |
| GE Millennium VG HEGP | 4.0                | 66               | 1.8                   |                        |                          |

and 9.5 mm) was also performed. Images were also evaluated qualitatively to assess the detection of the high-activity sphere in the abdominal torso phantom and other objects in the phantoms.

## RESULTS

The time–activity curves from the whole-body imaging sessions are shown in Figure 1. There was a clear separation between the curves for medium-energy (upper 3 curves) and high-energy (lower 2 curves) collimators, reflecting the different sensitivities of the collimators. Figure 2 shows the data from Figure 1 normalized to the counts at time 0 ( $A_0$  in Eq. 2), derived from the line-of-best-fit equation, for each  $\gamma$ -camera and collimator combination.

The half-lives measured from whole-body scans are shown in Table 5. The average measured half-life was 8.15 d (SD, 0.07 d), which is different by 1.6% from the NuDat database (7) reference value of 8.021 d. The average measured half-life for just the high-energy collimators was 8.12 d (SD, 0.11 d), and that for just the medium-energy collimators was 8.18 d (SD, 0.04 d). The half-life was not found by a Student  $t$  test to be statistically significantly different between the medium-energy and high-energy collimators ( $P = 0.44$ ). The observed half-life difference with crystal

thickness (8.09 d for 15.9 mm vs. 8.19 d for 9.5 mm) also was not found to be statistically significant ( $P = 0.06$ ).

To examine whether single-head  $\gamma$ -camera measurements had any impact on the measured  $^{131}\text{I}$  half-life, the same analysis was performed for anterior and posterior whole-body scans separately. Anterior and posterior  $^{131}\text{I}$  half-lives were calculated for anterior and posterior projections for each camera and collimator combination and are summarized in Table 6. For all camera and collimator combinations, the  $^{131}\text{I}$  half-life measured with the anterior head was 8.13 d (SD, 0.13 d), and that measured with the posterior head was 8.18 d (SD, 0.13 d). There was no statistically significant difference between the half-life measured with the  $\gamma$ -camera in the anterior orientation and that measured with the  $\gamma$ -camera in the posterior orientation ( $P = 0.6$  for all camera and collimator combinations,  $P = 0.52$  for MEGP, and  $P = 0.34$  for HEGP).

In  $^{131}\text{I}$ -tositumomab imaging, the administered therapeutic dose is determined by measurement of the TBRT with serial whole-body imaging. To investigate how medium-energy collimators affect the calculated administered therapeutic dose, we considered some data from a patient treated with  $^{131}\text{I}$ -tositumomab. For that particular patient receiving  $^{131}\text{I}$ -tositumomab therapy at our institution, the

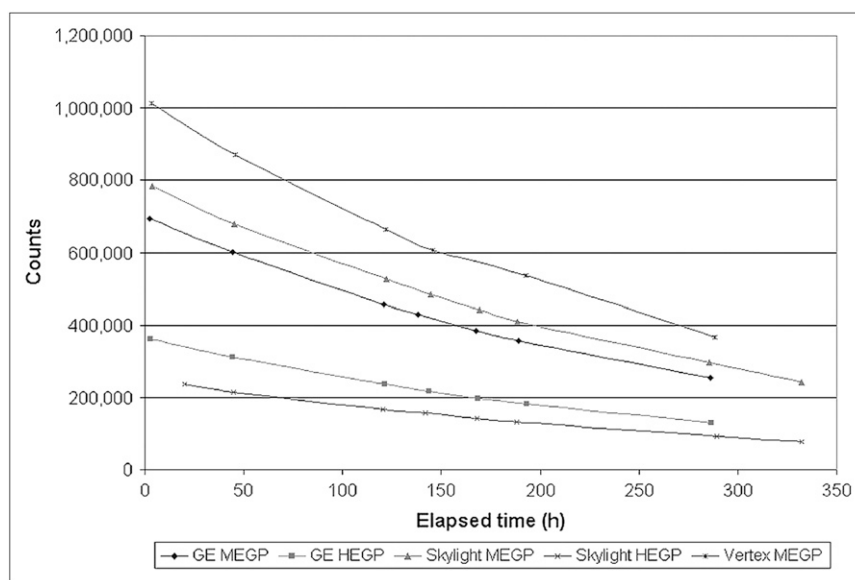


**FIGURE 1.** Time–activity curves from whole-body imaging.

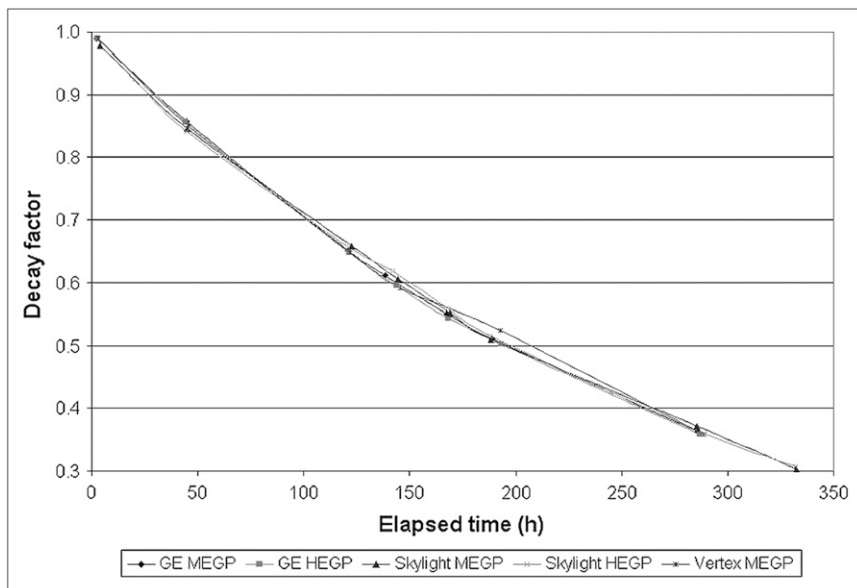


**FIGURE 2.** <sup>131</sup>I decay factors from whole-body measurements. Curves shown are data from Figure 1 normalized to activity at time 0 ( $A_0$  in Eq. 2), derived from line-of-best-fit equation.

measured TBRT was 114 h, corresponding to an effective half-life of 79 h. From this finding, the biologic half-life ( $t_B$ ) of <sup>131</sup>I-tositumomab can be determined as follows:

$$\frac{1}{t_B} = \frac{1}{t_E} - \frac{1}{t_P} \quad \text{Eq. 4}$$

In this equation,  $t_E$  is the effective half-life and  $t_P$  is the physical half-life. On the basis of a physical half-life of 192.5 h (8.021 d), the biologic half-life is 134 h.

Rearranging Equation 4 to produce Equation 5 and using the measured <sup>131</sup>I half-life for each collimator as the physical half-life, we calculated the effective half-life for each  $\gamma$ -camera and collimator combination (Table 7). Because  $t_P$  was larger than  $t_B$ , small changes in  $t_P$  were not expected to have a significant effect on  $t_B$  ( $1/t_P$  was small compared with  $1/t_B$ ), as shown by the following equation:

$$\frac{1}{t_E} = \frac{1}{t_P} + \frac{1}{t_B} \quad \text{Eq. 5}$$

Table 7 also shows the prescribed therapeutic dose of <sup>131</sup>I-tositumomab for the calculated TBRT values (range, 2.58–2.6 GBq).

**TABLE 5**

<sup>131</sup>I Half-Lives Measured from Whole-Body Scans

| Collimator       | <sup>131</sup> I half-life, d (% deviation from reference value) |
|------------------|--|
| GE Millennium VG |  |
| MEGP             | 8.135 (1.42)   |
| HEGP             | 8.042 (0.27)   |
| Skylight         |  |
| MEGP             | 8.175 (1.92)   |
| HEGP             | 8.194 (2.16)   |
| Vertex V60 MEGP  | 8.214 (2.41)   |

Whole-body images from the first day of phantom imaging with the GE Millennium VG are shown in Figures 3 and 4. On the left of each pair is the anterior image, and on the right is the posterior image. Qualitative comparisons between medium- and high-energy collimator images revealed several expected differences. The background in the medium-energy collimator images was much higher than that in the high-energy collimator images. In the medium-energy collimator images, the counts detected outside the phantom were attributable primarily to septal penetration. In both the medium- and the high-energy collimator images, the 2 spheres used to simulate altered biodistributions were clearly visible in the anterior and posterior projections. The visibility of the 3-cm sphere was slightly degraded in the anterior MEGP image compared with the anterior HEGP image, but the sphere was still easily detected.

## DISCUSSION

The simplified whole-body dosimetry method described by Wahl et al. (5) provides a direct means of performing <sup>131</sup>I-tositumomab dosimetry, which may be readily and accurately performed at institutions lacking expert technical

**TABLE 6**

<sup>131</sup>I Half-Lives Measured from Single-Head Acquisitions

| Collimator(s) | Anterior           |       |                 | Posterior          |       |                 |
|---------------|--------------------|-------|-----------------|--------------------|-------|-----------------|
|               | Mean half-life (d) | SD    | Difference* (%) | Mean half-life (d) | SD    | Difference* (%) |
| All           | 8.13               | 0.132 | 1.37            | 8.18               | 0.126 | 1.93            |
| MEGP          | 8.20               | 0.123 | 2.27            | 8.15               | 0.060 | 1.58            |
| HEGP          | 8.02               | 0.004 | 0.02            | 8.22               | 0.225 | 2.46            |

\*Between calculated half-life and reference value.

**TABLE 7**

<sup>131</sup>I-Tositumomab Effective Half-Life, TBRT, and Prescribed Therapeutic Dose for Patient, Calculated with Different  $\gamma$ -Camera and Collimator Combinations

| Parameter  | GE Millennium VG        |       | Skylight |       | Vertex V60 MEGP |
|------------|-------------------------|-------|----------|-------|-----------------|
|            | MEGP                    | HEGP  | MEGP     | HEGP  |                 |
|            | Effective half-life (h) | 79.5  | 79.1     | 79.6  |                 |
| TBRT (h)   | 114.7                   | 114.1 | 114.9    | 115.0 | 115.1           |
| Dose (GBq) | 2.59                    | 2.6   | 2.59     | 2.58  | 2.58            |
| Dose (mCi) | 70                      | 70.4  | 69.9     | 69.8  | 69.8            |

staff, who would otherwise be required to perform more involved quantitative dosimetry. Because <sup>131</sup>I is involved, institutions and clinics without high-energy collimators would normally be excluded from performing <sup>131</sup>I-based RIT procedures with the whole-body conjugate-view method. Our findings demonstrate that <sup>131</sup>I residence time measurements for RIT dosimetry can be obtained by use of cameras with medium-energy collimators without a significant loss of accuracy in determining TBRT.

Whole-body images for the clinical use of <sup>131</sup>I-tositumomab were also evaluated qualitatively to detect signs of altered biodistribution (i.e., altered liver or spleen uptake, thyroid uptake indicating free iodine or renal obstruction). Although <sup>131</sup>I imaging with medium-energy collimators does not produce the highest-resolution images, the <sup>131</sup>I-tositumomab imaging task is not one that requires high contrast or spatial resolution. Despite the production of lower-contrast images with medium-energy collimators, any alterations to the <sup>131</sup>I-tositumomab biodistribution significant enough to affect the clinical decision to administer the therapeutic dose should

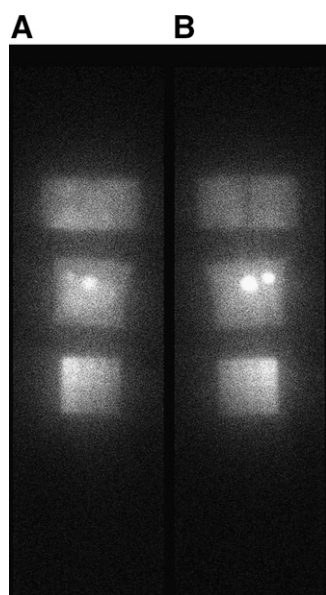


**FIGURE 3.** Anterior (A) and posterior (B) whole-body images from GE Millennium VG with MEGP collimator.

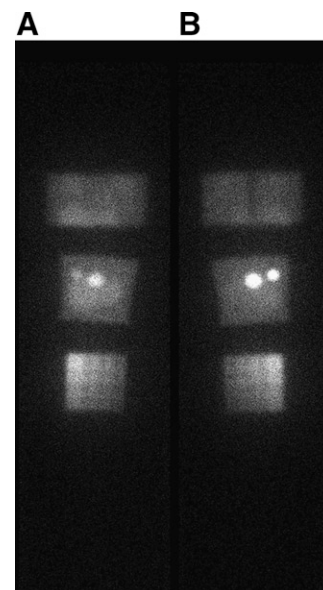


**FIGURE 4.** Anterior (A) and posterior (B) whole-body images from GE Millennium VG with HEGP collimator.

still be readily detected. This scenario is demonstrated by the visualization of the 3- and 6-cm spheres in the abdominal torso phantom. Image quality was better in the posterior image than in the anterior image (typical of whole-body scans, in which the posterior detector is usually much closer to the patient); therefore, for single-detector cameras, posterior whole-body imaging is recommended. The similarity in the measured half-life between anterior (8.13 d) and posterior (8.18 d) detectors also suggests that distance from the patient is not a significant factor in TBRT measurements.

**CONCLUSION**

Serial whole-body scans of 3 phantoms performed on 4 different  $\gamma$ -cameras with medium- and high-energy collimators yielded measured <sup>131</sup>I half-lives of 8.042–8.214 d. The mean half-life for all  $\gamma$ -camera and collimator combinations was 8.15 d (SD, 0.07 d). In single-head configurations, the results were similar, with measured half-lives of 8.13 d (anterior) and 8.18 d (posterior) for all  $\gamma$ -camera and collimator combinations. The measured half-lives at different crystal thicknesses were also similar (8.09 d for 15.9 mm and 8.19 d for 9.5 mm). These values are quite comparable to the reference value of 8.021 d from the NuDat database. The mean half-life measured with medium-energy collimators was 8.18 d, and that measured with high-energy collimators was 8.12 d; this difference is not statistically significant. The detection of altered biodistribution is not compromised when medium-energy collimators are used. On the basis of these results, for the purposes of measuring patient-specific TBRT and visual assessment of images to detect alterations in biodistribution, scanning patients administered <sup>131</sup>I-based RIT agents (such as <sup>131</sup>I-tositumomab) with medium-energy collimators is as accurate as scanning

with high-energy collimators in either single- or dual-head configurations.

## ACKNOWLEDGMENT

This work was supported in part by a grant from Glaxo-SmithKline.

## REFERENCES

1. Rajendran JG, Fisher DR, Gopal AK, Durack LD, Press OW, Eary JF. High-dose  $^{131}\text{I}$ -tositumomab (anti-CD20) radioimmunotherapy for non-Hodgkin's lymphoma: adjusting radiation absorbed dose to actual organ volumes. *J Nucl Med.* 2004;45:1059–1064.
2. Koral KF, Dewaraja Y, Li J, et al. Update on hybrid conjugate-view SPECT tumor dosimetry and response in  $^{131}\text{I}$ -tositumomab therapy of previously untreated lymphoma patients. *J Nucl Med.* 2003;44:457–464.
3. Autret D. Monte Carlo modeling of gamma cameras for I-131 imaging in targeted radiotherapy. *Cancer Biother Radiopharm.* 2005;20:77–84.
4. Green AJ, Dewhurst SE, Begent RH, Bagsawe KD, Riggs SJ. Accurate quantification of  $^{131}\text{I}$  distribution by gamma camera imaging. *Eur J Nucl Med.* 1990;16:361–365.
5. Wahl RL, Kroll S, Zasadny KR. Patient-specific whole-body dosimetry: principles and a simplified method for clinical implementation. *J Nucl Med.* 1998;39(suppl):14S–20S.
6. Juweid ME. Radioimmunotherapy of B-cell non-Hodgkin's lymphoma: from clinical trials to clinical practice. *J Nucl Med.* 2002;43:1507–1529.
7. National Nuclear Data Center, Brookhaven National Laboratory. NuDat 2.3 database [database on the Internet]. Available at: <http://www.nndc.bnl.gov/nudat2>. Accessed July 13, 2007.